A CAD system for nodule detection in low-dose lung CTs based on region growing and a new active contour model

R. Bellotti
Dipartimento di Fisica, Università di Bari; Sezione INFN di Bari, Italy
and Center of Innovative Technologies for Signal Detection and Processing (TIRES), Bari, Italy

F. De Carlo, G. Gargano,[a)] and S. Tangaro
Dipartimento di Fisica, Università di Bari; Sezione INFN di Bari, Italy

D. Cascio
Dipartimento di Fisica e Tecnologie Relative, Università di Palermo, Italy

E. Catanzariti
Dipartimento di Scienze Fisiche, Università di Napoli "Federico II," Italy

P. Cerello
Sezione INFN, Torino, Italy

S. C. Cheran
Dipartimento di Fisica, Università di Genova; Sezione INFN di Torino, Italy

P. Delogu
Dipartimento di Fisica, Università di Pisa, Italy

I. De Mitri
Dipartimento di Fisica, Università del Salento; Sezione INFN di Lecce, Italy

C. Fulcheri
Dipartimento di Fisica Sperimentale, Università di Torino, Italy

D. Grosso
Dipartimento di Fisica, Università di Genova; Sezione INFN di Genova, Italy

A. Retico
Sezione INFN di Pisa, Italy

S. Squarcia
Dipartimento di Fisica, Università di Genova; Sezione INFN di Genova, Italy

E. Tommasi
Dipartimento di Fisica, Università di Bari; Sezione INFN di Lecce, Italy

Bruno Golosio
Struttura Dipartimentale di Matematica e Fisica dell'Universitý di Sassari
and Sezione INFN di Cagliari, Italy

(Received 6 April 2007; revised 13 September 2007; accepted for publication 4 October 2007; published 28 November 2007)

A computer-aided detection (CAD) system for the selection of lung nodules in computer tomography (CT) images is presented. The system is based on region growing (RG) algorithms and a new active contour model (ACM), implementing a *local* convex hull, able to draw the correct contour of the lung parenchyma and to include the pleural nodules. The CAD consists of three steps: (1) the lung parenchymal volume is segmented by means of a RG algorithm; the pleural nodules are included through the new ACM technique; (2) a RG algorithm is iteratively applied to the previously segmented volume in order to detect the candidate nodules; (3) a double-threshold cut and a neural network are applied to reduce the false positives (FPs). After having set the parameters on a clinical CT, the system works on whole scans, without the need for any manual selection. The CT database was recorded at the Pisa center of the ITALUNG-CT trial, the first Italian randomized controlled trial for the screening of the lung cancer. The detection rate of the system is 88.5% with 6.6 FPs/CT on 15 CT scans (about 4700 sectional images) with 26 nodules: 15 internal and 11 pleural. A reduction to 2.47 FPs/CT is achieved at 80% efficiency. [DOI: 10.1118/1.2804720]

Key words: computer-aided diagnosis (CAD), image processing, computed tomography, image segmentation

I. INTRODUCTION

Lung cancer has the highest mortality rate of all cancers all over the world. In the U.S., 172 570 new cases and 163 510 deaths were reported in 2005.[1] The survival rate is estimated to be 14% after 5 years, with an increase up to 50% if the lung cancer is detected at an early stage.[2] The use of chest computer tomography (CT) strongly improves the radiologists' detection rate as well as the definition of the cancer type.[3] A CT exam consists of a series of 2D images (of about 150 MB when reconstructed with thin slice thickness) to be visually examined. This task is particularly difficult and time-consuming due to the fact that some nodules are hardly distinguishable from nonpathological structures (e.g., bifurcations of the vascular trees) when examined slice-wise. These facts have, in the last few years, encouraged the development of computer-aided detection (CAD) for the automated detection of lung nodules in CT scans. A CAD system could provide valuable assistance to the radiologists, and in many cases its use leads to a remarkable improvement of the detection rate at the cost of a low increase of the false positives (FPs).[4,5]

A number of CADs have already been brought to the attention of the scientific community. In order to give a brief and noncomprehensive overview of the state of the art, here we report some examples of CADs operating on CT scans.

In Ref. 6, a gray-level threshold routine is applied to both the 2D sections of a CT scan for automated lung segmentation, and the 3D segmented lung volume for individual structure identification. Nodule candidates are categorized as nodules or non-nodules by a combination of rule-based and linear discriminant classifiers applied on a set of features extracted from each candidate. A modified multilayer artificial neural network, capable of operating on image data directly, is applied to 63 low-dose CT scans (1765 slices) containing 71 nodules: a detection rate of 80.3% is obtained with 0.18 FPs/slice, corresponding to 4.8 FPs/CT.

The CAD presented in Ref. 4 uses three-dimensional segmentation involving attenuation thresholding, region growing, and mathematical morphology to identify the regions of interest. The system labels these regions on the basis of a model of lung nodules and relevant intrathoracic anatomy. When applied to a set of eight low-dose CTs (40 slices/CT) containing 22 nodules, the system achieves a detection rate of 86.4%, with 2.64 FPs/CT.

The CAD system of Ref. 7 relies on a *k*-means clustering technique for the segmentation of both the lung region and the anatomical structures. Then, rule-based classifiers are designed to distinguish lung nodules from normal structures using 2D and 3D features. Linear discriminant analysis is used to further reduce the number of FPs. A preliminary study performed on 1454 slices from 34 CTs with 63 lung nodules provides 84% (53/63) efficiency, with 1.74 (2530/1454) FPs/slice.

A template-matching technique based on a genetic algorithm is proposed in Ref. 8. The genetic algorithm is used to locate the target position in the image and to select an adequate template image from several reference patterns for quick template matching. In addition, a template matching is employed to detect the nodules on the lung wall area. After the initial detection of candidates, 13 features are extracted and used to reduce the FPs by means of a rule-based mechanism. A number of the 557 sectional images are selected from 20 clinical cases, and 71/98 (about 72%) are correctly detected, with approximately 1.1 FPs/slice.

The approaches presented in Ref. 9 are based on the radial gradient index. A database of 38 CT scans is used, comprising 1953 sections and containing 82 nodules. For each CT section, regions of high circularity are enhanced to improve the contrast between nodules and nonpathological structures. The application of filters prior to a linear discriminant classifier yields 70% sensitivity with 0.28 FPs/section.

Among the commercial CADs, ImageCheckerCT of R2 Technology Inc. (Sunnyvale, CA) is the first clinically validated system. The CAD works as follows: a series of volume-centric segmentation steps is used to delineate normal from abnormal lung tissue. Geometric features, including shape, elongation, size, spiculation, density, and others, are computed for each suspected lesion. Following an analytical decision tree, the candidate lesion is given a likelihood rating of representing a lung lesion. If this score exceeds a defined threshold, the CAD system marks the region of interest (ROI) for further review. The use of this CAD leads to improved detection as validated by independent clinical studies: 26% reduction in missed actionable nodules, with an average of 2 FPs per case, is observed in a multireader ROC (receiver operating characteristic) study.[5] In addition, the ImageChecker CT detects nodules of clinical significance in 23% of multislice CT chest exams originally read as having no nodules.[10]

As one can see, a variety of methods has been explored with promising results, yet the problem of detecting lung nodules in CT scans is still open and of great interest. In this paper we present a CAD system for the detection of lung nodules in a CT exam. This work has been developed in the framework of the MAGIC-5 Project,[11] which aims at implementing CAD software for medical applications on a grid infrastructure connection.[12] The system is based on region growing (RG) algorithms and a new active contour model (ACM),[13] implementing a *local* convex hull (CH), able to draw the correct contour of the lung parenchyma and to include the pleural nodules, i.e., nodules near the pleura. The CAD consists of three main modules: (1) lung parenchymal volume segmentation; (2) nodule candidate detection; and (3) FP reduction.

The paper is organized as follows. In the next section the CT database is described. Section III is focused on the description of the two computational methods of image analysis used in our CAD: region growing (RG) and active contour model (ACM). In Secs. IV–VI the CAD modules are described in detail. Results and comments are provided in Sec. VII.

II. THE CT DATABASE

Chest computer tomography (CT) is considered the best imaging modality for the detection of lung nodules. In the

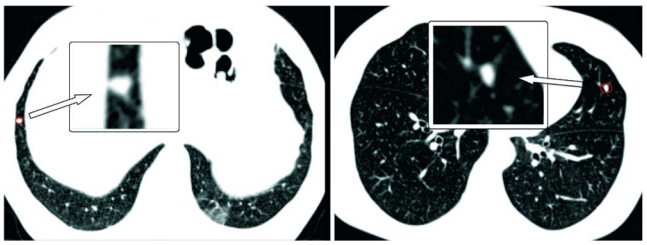

FIG. 1. Two typical examples of nodules present in our database: pleural nodule (left) and internal nodule (right).

last few years, low-dose CT scans were shown to be effective for the analysis of the lung parenchyma,[14] thus making possible the perspective of screening programs.

The database used in this study consists of 15 low-dose CT (LDCT) scans recorded with a 4-slice spiral scanner Somatom Plus 4 VZ machine, with the following settings: 140 kVp, 20 mA, 1.25 mm collimation, and 1 mm reconstruction interval. The images were acquired at the Pisa center of the ITALUNG-CT trial, which is the first Italian randomized controlled trial for the screening of lung cancer. Each image consists of a matrix of $512\times512\times(314\pm23)$ voxels: it should be stressed that both the number of the voxels and their longitudinal size depends on the patient size.

The scans contain 26 nodules: 15 internal nodules (i.e., far from the pleura) and 11 pleural nodules (i.e., near the pleura). Figure 1 shows two typical examples of nodules present in our database: pleural nodule (left) and internal nodule (right). The CT examinations were carried out independently by two radiologists by means of slice-wise visual inspection. The nodules were diagnosed according to the ITALUNG protocol that considers as pathological, structures of noncalcified nodules with a diameter greater than 5 mm, up to a maximum diameter of about 14 mm. Hence, the pathological structures searched by the radiologists of the ITALUNG-CT trial are objects of volume $V\in[30, 800]$ in terms of number of pixels. The presence of a nodule is marked by a circle which completely encloses the nodule in its median slice. The mean diameter of the nodules in the whole database is $d=(6.7\pm1.5)$ mm.

III. METHODS

In this section we give a general overview of the two principal algorithms used in our CAD: region growing (RG) and active contour model (ACM).

III.A. Region growing

The RG is an image analysis technique that consists of searching for connected regions of pixels satisfying a given inclusion rule. The algorithm works as follows:

(1) A *seed* point is chosen and its neighbors are considered;
(2) If the neighbors satisfy the inclusion rule, they are included in the growing region, otherwise they are ruled out;
(3) All points included at a certain step become seed points for the following step;
(4) The routine is iterated until no more points satisfy the inclusion rule.

The main problem of a RG algorithm relies in the selection of a proper seed point, which is usually done by hand. As our aim is the implementation of an automated CAD system, the seed point could be automatically selected (as in the nodule candidate detection phase, Sec. V) as follows: a scan of the 3D matrix is carried out and the first voxel satisfying the inclusion rule is chosen to start the growth. When the growth is finished, the segmented region is removed from the image and the matrix scan restarts to search for a new seed point. This routine is iterated until no more seeds are found. In this way, a number of not-connected regions satisfying the same inclusion rule is obtained.

Different inclusion rules may be adopted. We use the following ones:

(1) Simple Bottom Threshold/Simple Top Threshold (SBT/STT): If the intensity I is greater/lower than a certain threshold θ, the voxel is included in the growing region:

$$I \geq \theta \ \text{(SBT)},$$

$$I \leq \theta \ \text{(STT)}.$$

(2) Mean Bottom Threshold/Mean Top Threshold (MBT/MTT): The intensities of the voxel and its 26 neighbors are averaged; if the average $\langle I\rangle$ is greater/lower than the threshold θ, the voxel is included in the growing region:

$$\langle I\rangle \geq \theta \ \text{(MBT)},$$

$$\langle I\rangle \leq \theta \ \text{(MTT)}.$$

III.B. Active contour model

The active contour model (ACM), first introduced in Ref. 15, is an image analysis technique used to define the contours of complex objects. The focus of this technique consists of positioning a closed curve, a *spline*, joining a number of nodes, in a certain position of the image, and leaving it to evolve until an equilibrium position is reached. The evolution of the spline is driven by both internal forces (generally elastic forces) attracting (or repelling) the nodes to (or from) one another, and external forces based on the image suitably transformed into a potential or a force field. Different results can be obtained depending on the initial position of the spline and on the kind of transformation of the image. ACMs are used in many fields as tracking of moving objects for traffic monitoring,[16] facial feature extraction,[17] or, as in our case, in medical image analysis for anatomical contour selection.[18]

IV. LUNG VOLUME SEGMENTATION

The first step of the CAD system is the parenchymal volume segmentation. This step consists of two substages:

(1) Internal lung volume segmentation by means of a RG algorithm;

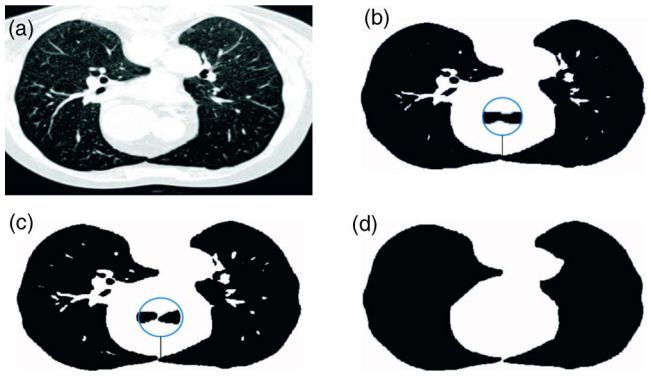

FIG. 2. (a) Original section of a CT scan: low-intensity (black) voxels correspond to air and bronchial tree; high intensity voxels correspond to pleura, fat, muscles, vascular tree, bones and, eventually, nodules. (b) Section of the volume segmented by the MTT RG; an enlargement of the two lungs joined together is displayed in the circle. (c) the same slice as in (b) with separated lung sections, as displayed by the enlargement in the circle. (d) A section of the *working volume*, obtained after the ACM contour detection.

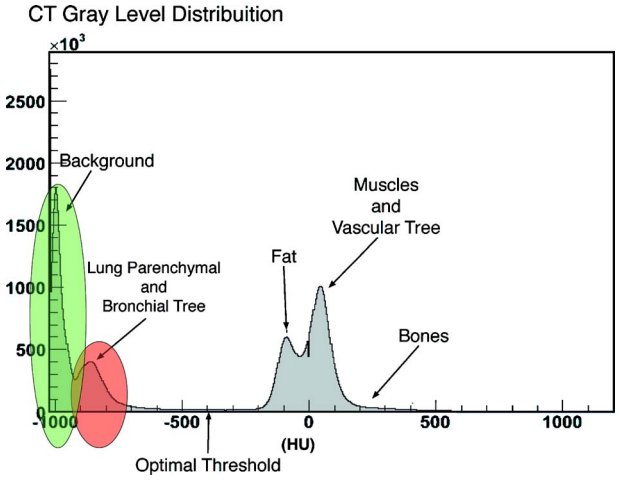

FIG. 3. Gray-level distribution of the voxels of one of the analyzed CT. Similar distributions can be obtained from the other CTs. The region segmented by the RG algorithm refers to the lung parenchymal and the bronchial tree. The voxels corresponding to the background, though having an intensity lower than the threshold $\bar{\theta}$, are not included in the grown region because they are not geometrically connected with the seed point.

(2) Anatomic lung contour detection, to include both the pleural nodules and the vascular tree inside the lung, implemented slice-wise by the new ACM, called the glued elastic band (GEB).[13]

IV.A. Internal lung volume segmentation

The internal lung volume consists of air and a bronchial tree that typically appears, in a CT slice, as low-intensity voxels surrounded by high-intensity voxels corresponding to the pleura (see Fig. 2(a)]. This suggests segmenting the internal lung volume by means of a 3D RG algorithm. The choice of the inclusion rule with the optimal threshold and the selection of a proper seed point are of great relevance for the best performance of the algorithm. Our choice is the MTT rule that allows reduction of the "noise" of the low-dose CT, thus obtaining a volume with quite regular contours.

The threshold value $\bar{\theta}$ is automatically selected with the method adopted in Ref. 19; it is based on the gray-tone distribution of the CT voxels that typically shows two quite distinct parts (see Fig. 3, obtained from one of the analyzed CTs): one containing air, lung parenchyma, trachea, and bronchial tree; the other one containing vascular tree, bones, muscles, and fat. The optimal threshold, set at the *plateau* between these two regions, is selected as follows:

- The CT gray-tone histogram is divided into two regions with equal number of bins and the mean values of the bins in the two regions are computed;
- The previously computed mean values are averaged and the bin having the intensity nearest to the new mean is selected as the threshold to divide the histogram;
- The routine is iterated until the threshold bin does not change anymore.

The seed point of the RG is automatically selected as the first voxel that satisfies the inclusion rule in a cubic region located as follows: the CT is divided lengthwise, thus obtaining two parts of equal sizes; the center of the cube is positioned at the cross point of the diagonals of, say, the left part (the choice of the right part would be equivalent). In this way, we are quite sure that the cubic region where the seed point is searched is inside the lung for less than abnormal anatomical deformities. Once this voxel is found, the growth of the internal lung volume is started; otherwise, the search is repeated in a greater cubic region until a voxel satisfying the inclusion rule is found.

The volume thus segmented shows some slices with joined lungs (see the magnified circle in Fig. 2(b)). To draw the correct lung volume contour (see Sec. IV B), it is necessary that the two lung sections are separated in all slices. To this purpose, a lower number of voxels should be included in the growing region, along the contour of the sections where the lungs are joined. This is achieved as follows:

(1) Starting from the top, the slices where the lung sections are joined are found, and a 2D RG is carried out in each slice with MTT inclusion rule and 1% decreased threshold with respect to the initial value $\bar{\theta}$.
(2) The threshold is decreased at the same rate in order to include a lower number of voxels into the 2D growing region, until the lung sections are disjoined.

The previously described routine is repeated for all slices where the lung sections are joined. As an example, Fig. 2(c) shows the result (see the magnified circle) of the above-described routine when applied to the image displayed in Fig. 2(b).

Figure 4 shows another typical example of one slice of the segmented region. It should be stressed that the volume thus obtained includes the lung parenchyma, the bronchial tree, and the trachea, while structures outside the lung, as bones, fat, and vascular tree are ruled out. Also, internal and pleural

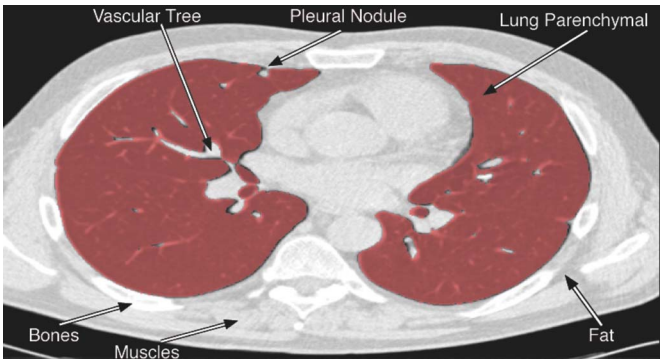

FIG. 4. An example of one slice of the internal lung volume obtained after the first step of our CAD. It should be stressed that the presence of a pleural nodule has not been included in the segmented region.

nodules are not included at this stage because they do not satisfy the MTT inclusion rule. On the other side, not only the nodules but also the vascular tree inside the lung must be included in the parenchymal volume, because there may be some nodules attached to its external walls. To this purpose, the contour of the lung must be outlined and all voxels inside this contour must be considered.

IV.B. 2D anatomic lung contour detection: The GEB algorithm

The anatomic lung contour selection is implemented slice-wise; after that, all pixels inside the 2D contours will be combined together to obtain the 3D segmented volume. Figure 5(a) shows an example of segmented lung slice, as obtained with the RG, together with the contour of the lung section. As one can see, the lung slice includes a pleural nodule, marked by the black circle, that is ruled out by the contour. To avoid this drawback one might think of applying

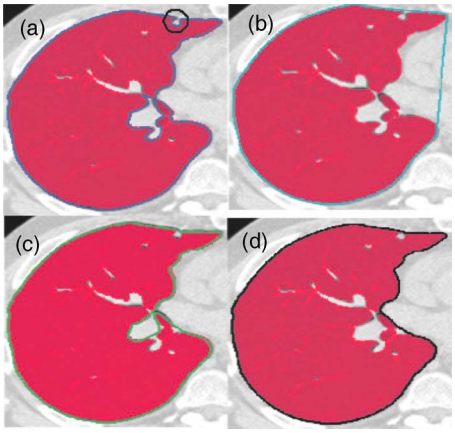

FIG. 5. (a) The 2D lung contour obtained after the segmentation with the RG: the pleural nodule, marked by a circle, is ruled out; this contour is the initial position of the spline in the GEB dynamics and corresponds to the case $q=+\infty$; (b) the 2D lung contour obtained with a CH: the pleural nodule is included in the contour but the right part of the lung is roughly approximated by a straight line; this contour is also obtained by the GEB dynamics for $q=0$; (c) the 2D lung contour obtained by the GEB with a suboptimal value of the parameter q; (d) the 2D lung contour obtained by the GEB with the best value of q.

a convex hull (CH) algorithm, which is the intersection of all convex regions containing a given object. The result of such application is shown in Fig. 5(b): the pleural nodule is correctly included in the contour but other concave structures, such as the section of the vascular tree near the lung hilum, are roughly approximated by a straight line.

Other approaches can be followed for the detection of the pleural nodules, as comparing the curvatures at points on the lung border:[20] a rapid change in curvature indicated a nodule, large vessel, or bronchus that formed an acute or obtuse angle with the lung border, and the lung border was then corrected by means of insertion of a border segment.

We have developed a new kind of ACM algorithm, called *glued elastic band* (GEB),[13] that simulates the dynamics of a spline *glued* to the nodes along the contour. The algorithm implements a sort of *local* CH, able to include concave parts with little bending radius, such as pleural nodules, and to rule out concave parts with great bending radius, such as the section of the vascular tree near the lung hilum. The algorithm relies on one parameter, q, that can be considered as the quantity of glue. The results are shown in Figs. 5(c) and 5(d): in particular, Fig. 5(c) shows the results obtained with a nonoptimal value of q, while Fig. 5(d) shows the lung contour obtained with the optimal quantity of glue. As one can see, the spline has reached an equilibrium position that includes concave parts with little bending radius as pleural nodules, while concave parts with great bending radius, as the section of the vascular tree near the lung hilum, are ruled out.

The RG segmentation is a necessary step to properly initialize the GEB spline in an automatic way. The initial position of the spline corresponds to the 2D contour obtained after the RG segmentation: each pixel of the 2D contour is a node of the spline; otherwise, the initial position of the spline should be set manually. The dynamics of the spline is driven by the following forces:

(1) Constant internal forces where the nodes exchange one another with the nearest neighbors (the previous and the following along the spline).
(2) Constant adhesive forces acting toward the inside of the object when the nodes are in contact with the section contour of the object, as if there was some glue on the spline.
(3) The constraint reactions acting when the nodes are pushed inside the contour.

In detail, let us consider the constant internal forces $\vec{F}_{i+1}$ and $\vec{F}_{i-1}$ acting on node i due to the neighboring nodes $i+1$, $i-1$; if a Cartesian system is considered with origin on the node i and axis versors $\vec{u}_x$ and $\vec{u}_y$, we have

$$\begin{cases} \vec{F}_{i-1} = \cos\ \vartheta_{i-1}\vec{u}_x + \sin\ \vartheta_{i-1}\vec{u}_y \\ \vec{F}_{i+1} = \cos\ \vartheta_{i+1}\vec{u}_x + \sin\ \vartheta_{i+1}\vec{u}_y, \end{cases} \tag{1}$$

where the angles ϑ_{i-1} and ϑ_{i+1} define the directions of the neighboring nodes with respect to node i. The resultant in-

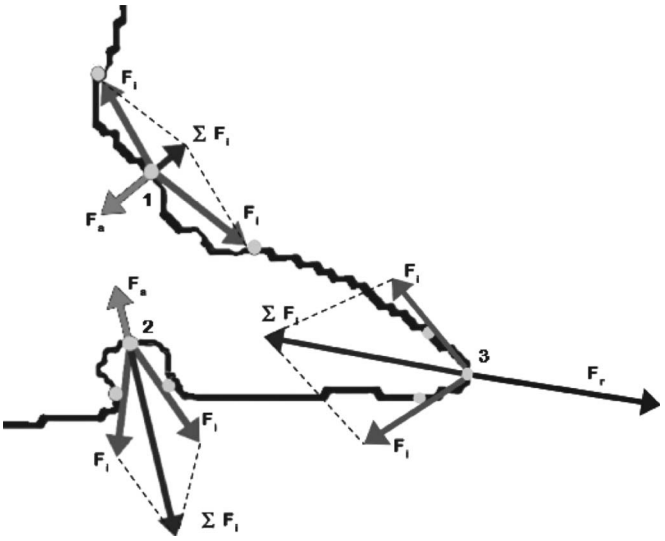

FIG. 6. A pictorial explanation of the GEB dynamics: node number 1 is on a concave part of the contour with great bending radius where the sum of the internal forces, due to nearest neighbors, is smaller than the adhesive force due to the glue; hence, such node remains glued to the contour: this is the typical case of the nodes near the lung hilum. Node number 2 is on a concave part of the contour with little bending radius where the sum of the internal forces is strong enough to exceed the adhesive forces; the effect is that the spline is pulled out and the concave part is included inside the spline: this is the typical case of the pleural nodules. For node number 3 the sum of the internal forces points toward the inside of the region: such node feels a constant reaction as for an object on a plane; the effect is that this node does not move. This dynamic is applied to all nodes of the spline.

ternal force on node i has the following intensity and orientation:

$$|R_i| = \sqrt{(\cos\,\vartheta_{i-1} + \cos\,\vartheta_{i+1})^2 + (\sin\,\vartheta_{i-1} + \sin\,\vartheta_{i+1})^2}, \quad (2)$$

$$\tan\,\vartheta_{R_i} = \frac{\sin\,\vartheta_{i-1} + \sin\,\vartheta_{i+1}}{\cos\,\vartheta_{i-1} + \cos\,\vartheta_{i+1}}. \quad (3)$$

The adhesive force $\vec{F}_a$ due to the glue is assumed to have the same direction as $\vec{R}_i$, versor pointing always toward the inside of the contour, and constant strength $|F_a|$. If the sum $\vec{F}_{\mathrm{tot}_i} = \vec{R}_i + \vec{F}_a$ points toward the outside (R_i and F_a have opposite versor, with $|\vec{R}_i| > |\vec{F}_a|$), node i detaches from the contour. If $\vec{F}_{\mathrm{tot}_i}$ points toward the inside ($\vec{R}_i$ and $\vec{F}_a$ have the same versor), then a constraint reaction $\vec{N}_i$ (equal strength and direction of $\vec{F}_{\mathrm{tot}_i}$, opposite versor) forbids node i to move inside the contour: as a result the node remains glued to the contour. Figure 6 provides a pictorial explanation of this dynamics: for nodes on concave parts of the contour with great bending radius, as node number 1, the sum of the internal forces, due to nearest neighbors, is smaller than the adhesive force due to the glue; hence, such nodes remain glued to the contour: this is the typical case of nodes near the lung hilum. On the other side, for nodes on concave parts of the contour with little bending radius, as node number 2, the sum of the internal forces is strong enough to exceed the adhesive forces of the glue; the effect is that the spline is pulled out and the concave part is included inside the spline: this is the typical case of the pleural nodules. Finally, for node number 3 the sum of the internal forces points toward the inside of the region: such node feels a constant reaction as for an object on a plane; the effect is that this node does not move. This dynamics is applied to all nodes of the spline.

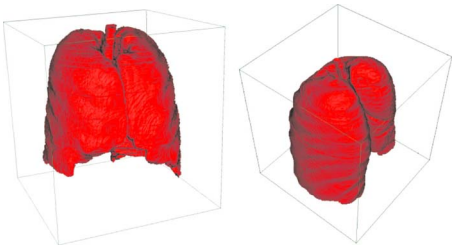

FIG. 7. 3D images obtained as a result of the segmentation step. The segmented volume is reduced to about 15% of the total volume of the original CT scan, and about 25% of the chest volume.

The only parameter of the GEB is quantity of glue that is given by the ratio between adhesive and internal forces,

$$q = \frac{F_a}{F}. \quad (4)$$

It is interesting to note that in the limit $q = +\infty$, the internal forces are irrelevant with respect to the adhesive forces, and the spline remains perfectly glued to the 2D contour: this case corresponds to the initial position of the spline [Fig. 5(a)]. On the other side, for $q=0$, the adhesive force is zero and the result is the same as a CH [Fig. 5(b)]. Between these two cases, one can have intermediate values implementing a *local* CH with different results: the higher the q, the greater the bending radius of the concave parts that are ruled out. The parameter q is set slice-wise by varying its value until the following condition holds:

$$\frac{A_i}{A_f} = a, \quad (5)$$

where A_i and A_f are, respectively, the initial and the final area inside the 2D contours. The parameter a has been optimized in order to maximize the number of the nodules included in the contour and minimize the segmented volume. This optimization has been carried out on one clinical CT containing many pathological structures of different types and sizes. Then, its value is the same for all 15 test CTs. However changes of a in the neighborhood of the best value do not affect in a substantial way both the number of detected nodules and the volume of the segmented region, thus suggesting that the method is stable.

All voxels inside the final position of the spline are considered [see Fig. 2(d)] and, combining together the regions inside the 2D contours of each slice, we obtain the 3D segmented volume which contains bronchial and vascular trees inside the lung, trachea, internal, and pleural nodules. Nodules will be searched inside this *working volume*. Figure 7 shows two 3D images obtained as a result of the segmentation step. The volume thus segmented is reduced to about 15% of the total volume of the original CT scan, and about 25% of the chest volume, and no nodule is missed.

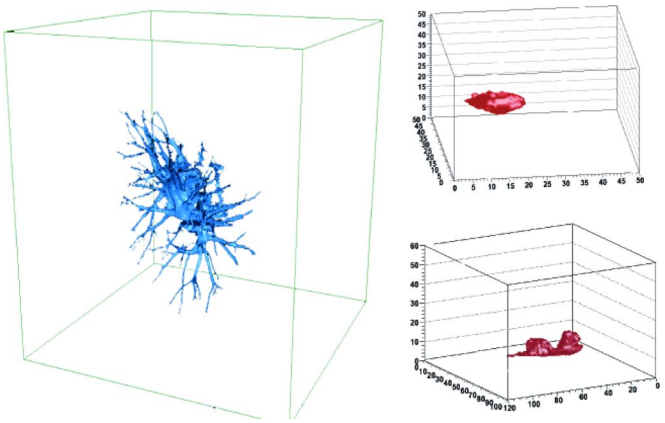

FIG. 8. Examples of the structures found by the CAD system: part of the vascular tree (left) and nodules (right).

V. NODULE CANDIDATE DETECTION

The second step of the CAD system consists of detecting the candidate nodules inside the working volume. This is implemented by a RG algorithm with an inclusion rule given by the AND combination of MBT and SBT rules. The thresholds are chosen in order to maximize the detection rate (or sensitivity, or efficiency) defined as the fraction of selected nodules with respect to the total number of nodules diagnosed by the radiologist. This optimization is carried out on the above-mentioned clinical CT. The seed points are searched automatically as follows: the segmented volume is scanned until a voxel satisfying the inclusion rule is found; this voxel is used as seed point and the growth is started. Once the region is completely grown, it is removed from the CT and stored for further analysis. Then, the search for new seed points is restarted. The routine is iterated until no more seed points satisfying the inclusion rule are found. Some examples of the structures found by the CAD system are shown in Fig. 8. To assess the efficiency of this step, we define as *true positives* (TPs) the candidate nodules that meet the radiologists' diagnosis according to the following condition:

$$\begin{cases} |X_{\mathrm{rad}} - X| < R_{\mathrm{rad}} \\ |Y_{\mathrm{rad}} - Y| < R_{\mathrm{rad}} \\ |Z_{\mathrm{rad}} - Z| < R_{\mathrm{rad}} \end{cases},$$

where $\{(X_{\mathrm{rad}}, Y_{\mathrm{rad}}, Z_{\mathrm{rad}}), R_{\mathrm{rad}}\}$ are the center coordinates and the radius of the radiologists' drawn circle, and $\{(X,Y,Z),R\}$ are the same quantities of the CAD candidate nodule. All other candidates are considered as false positives (FPs).

With the above-mentioned definitions, the efficiency of the nodule hunter on 15 CTs containing 26 nodules (15 internal and 11 pleural) is 88.5% (23/26), with about 2775 FPs/CT.

VI. FP REDUCTION

Almost all FP findings refer to candidates with too many or too few voxels, and can be easily ruled out by a simple double-threshold cut on the volume V (expressed in number of voxels). As mentioned in Sec. II, the structures diagnosed by the radiologists of the ITALUNG-CT trial have diameters of about $5 \leq d \leq 14$ mm, corresponding to volumes $V \in [30, 800]$, expressed in terms of voxels. Hence, we exploit this *prior* information to rule out all findings with volume out of this range, thus reducing the false positives obtained by the nodule hunter. As a result of this volume filter the efficiency is preserved (88.5%), while FPs are reduced to 722 corresponding to 48.1 FPs/CT. It should be stressed that the values of the thresholds arise from the diagnosing setting of the ITALUNG-CT trial and do not rely on the structures found by the nodule hunter. Moreover, the stability of the CAD performance has been checked for different values of the thresholds in proximity of the above-mentioned values ($V_{\mathrm{min}}=30$ and $V_{\mathrm{max}}=800$). Consequently, the results we will report in the following are the same for different thresholds close to the reported values.

A further reduction of the FPs can be obtained by means of a classification step carried out by a supervised two-layered (three inputs, seven hidden neurons, and one output) feed-forward neural network, trained with gradient descent learning rule[21] (learning rate: $\eta=0.01$) with momentum[22] (momentum term: $\alpha=0.9$), and sigmoid transfer function (*gain factor* $\beta=1$). These parameters have been set in order to obtain the best classification performance in term of area under the ROC curve (AUC). The input features are as follows:

(1) Volume, V.
(2) Roundness, $R=V/V_S$, where V_S is the volume of the smallest sphere containing the segmented region.
(3) Radius r, defined as the mean distance between the nodule center and the contour points.

The *leave-one-nodule-out cross validation*[23] is used to exploit the highest possible number of TPs during the training phase. The name of this strategy refers to the fact that one TP patterns is, in turn, left out and used for validating the network while the other ones are used for the training. As far as the FPs are concerned, a subset of proper size must be selected to suitably train the network. After different trial-and-error approaches, we use all 23 TPs and 69 FPs for the training phase and we proceed as follows:

- The 69 FPs are extracted with a probability given by the distribution of all 722 FPs, in space spanned by the above-mentioned features (volume, roundness, radius); in this way we are sure that the FP patterns used for training the network are representative of all FPs.
- The patterns (23 TPs+69 FPs) are randomly divided into 23 sets, each one with 1 TP and 3 FPs.
- Twenty-two out of 23 sets are put together for training the network, while the last one is used for validation: in this way a neural output is assigned to each pattern of the validation set.
- A cyclical permutation of the sets is carried out: for each permutation the network is trained with 22 sets and validated on one set; in this way a neural output is assigned to all patterns.

- The remaining 653 FPs, not selected for the cross validation, are divided into 23 subsets; each subset is classified by one of the 23 networks.

As a consequence of this routine, a neural output is assigned to all 23 TPs and 722 FPs and used to draw the ROC and FROC curves.

A quite similar cross-validation approach can be adopted: the *leave-one-CT-out*, instead of the *leave-one-nodule-out*. The former is suitable when texture-based features are used for characterizing the nodules: in this case, the similar texture of a CT might cause a bias if nodules from the same CT are partly in the training set, partly in the validation one. This is not the case in our processing, for which the latter approach is the best one, due to the fact that it exploits the greatest possible number of TP patterns for the training phase, without introducing any bias.

The neural outputs give rise to a two-class distribution in the range $[0,1]$, with target $t=1$ for TPs, $t=0$ for FPs. Given the neural distributions, the ROC curve is drawn as follows:

(1) A decision threshold $k \in [0,1]$ is fixed such that the efficiency is defined as the number of TPs with neural output greater than k; the specificity is the number of FPs with neural outputs lower than k; the FP rate is given by 1-specificity. In this way a fixed value of k defines a point (efficiency; FP rate) in the ROC plane.
(2) The threshold is shifted in the $[0,1]$ interval with step 0.01, such that 101 points are obtained.
(3) The ROC curve is the set of such points; for a better visual impact and for the computation of the area under the curve, a solid line joining the points is drawn.

The same procedure is carried out to draw the FROC curve with the following differences:

- The efficiency (or sensitivity) is computed with respect to the radiologists' drawn circles (diagnosis), thus having a maximum possible value given by the efficiency of the nodule hunter.
- The number of FPs per CT is reported on x axis instead of the FP rate.
- Differently from the ROC curve, the FROC curve is displayed without joining the points: in such a way one can focus on a particular working point (efficiency; FP/CT) and compare the performance with other CADs.

VII. RESULTS AND COMMENTS

Figure 9 displays the ROC curve[24] assessing the neural network capability in classifying the nodule candidates. The AUC is $A_z=0.969\pm0.027$, where the error is computed as reported in Ref. 25. Figure 10 shows the FROC curve which provides the performance of the overall CAD system in detecting the nodule, thus valuating also the effectiveness of the lung volume segmentation, the nodule candidate searching, and the FP reduction mechanism. As one can see from Fig. 10 the use of the neural network allows reduction of the number of FPs/CT from 48.1 to 6.6 without reducing the overall efficiency (88.5% as obtained after the double-threshold cut). A further reduction to 2.47 FPs/CT can be obtained at a lower detection rate (80%).

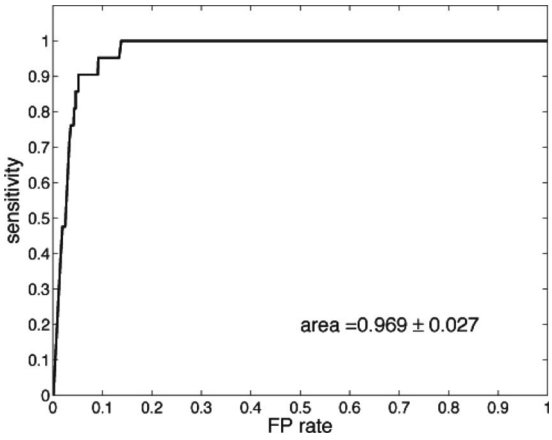

FIG. 9. Neural network ROC curve reporting the sensitivity (fraction of positive nodule candidates correctly classified) against the FP rate (fraction of FP nodule candidates classified as positive), at different values of the decision threshold on the neural network output.

A summary of the results achieved by other CADs is reported in Table I. A direct comparison is unfeasible, due to the following reasons:

(1) The databases differ for the number of CT scans, the number of slices per CT, and the dose of the images (in some cases this information is missing).
(2) The starting points of the processing systems are different: our CAD processes the whole CT and automatically extracts the slices to analyze; the other CADs rely on a manual selection of the sectional images.
(3) The results are provided in different ways: in particular, FPs are given per slice or per CT (it should be stressed that, in general, FPs/CT is different from FPs/slice multiplied by the number of slices/CT).

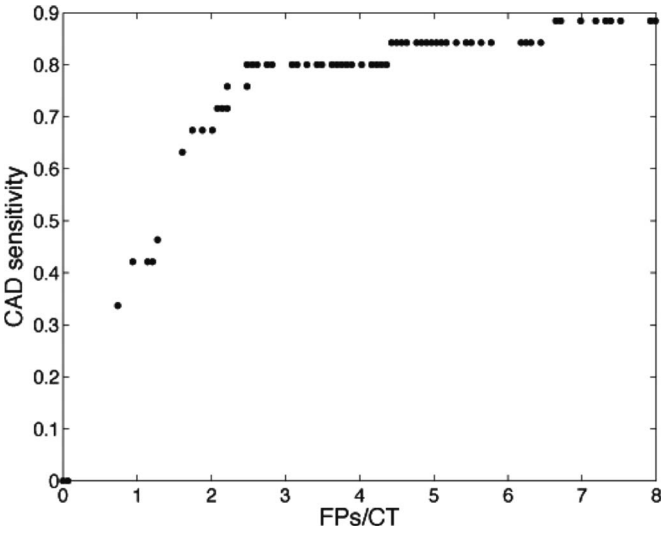

FIG. 10. Overall CAD FROC curve reporting the sensitivity, evaluated with respect to the radiologists' diagnosis, against the FPs/CT.

TABLE I. Review of the results reported by other CADs.

CAD	Scans	Dose	Slices/CT	Nodules	Efficiency	FPs/slice	FPs/CT
Ref. 4	8	low	40	22	86.4%	-	2.64
Ref. 6	63	low	~28	71	80.3%	0.18	4.8
Ref. 7	34	-	~43	63	84%	1.74	-
Ref. 8	20	-	~28	98	72%	1.1	-
Ref. 9	38	-	~51	82	70%	0.28	-
Our CAD	15	low	~314	26	88.5%	-	6.6
					80%		2.47

(4) Some CADs focus their analysis on the dimension of the nodules, thus providing detection rates at different nodule sizes.

Some considerations can be outlined. Though our CT database is smaller than the other ones (except the case of Ref. 4), the number of analyzed sectional images is the greatest one, due to the fact that the whole CTs are processed, with no need for a manual selection of the slices. This fact represents one of the main contributions of the proposed CAD and is of great importance in view of developing a prototype CAD system that can be used in a clinical routine directly by the radiologists of the hospitals belonging to the MAGIC-V Collaboration. Despite the almost completely automated computing chain, we obtain good values of both efficiency and FPs/CT.

VIII. CONCLUSIONS

The nodule detection in lung CT scans is a hard task due to the fact that a sequence of slices must be analyzed. From this point of view, the CAD systems can be a useful tool to help the radiologists for lung cancer diagnosis. We have developed a CAD system which consists of three steps: (1) segmentation of the lung parenchymal volume and inclusion of the pleural nodules; (2) nodule candidate detection; (3) FP reduction. The techniques of the image analysis used to implement the first two steps of the CAD system are the region growing, for lung segmentation and nodule searching, and a new active contour model, implementing a sort of *local* convex hull for the inclusion of the pleural nodules. The FP reduction is obtained by means of double-threshold cut and a neural network classifier. The parameters of the CAD have been set on a clinical CT containing many pathological structures of different types and sizes. The system has been evaluated on a database of 15 CT scans with 26 nodules: 15 internal and 11 pleural. A detection rate of 88.5% is achieved with 6.6 FPs/CT, or 80% with 2.47. The almost complete automatization of our CAD suggests that it can be used as a valuable support to the radiologists for the diagnosis of lung nodules in low-dose CT scans.

ACKNOWLEDGMENTS

The authors thank Dr. L. Battolla, Dr. C. Spinelli, and Dr. F. Falaschi of U.O. Radiodiagnostica 2, Azienda Ospedaliera Universitaria Pisana; Professor D. Caramella and Dr. T. Tarantino of Diagnostic and Interventional Radiology of University of Pisa.

[a]Author to whom correspondence should be addressed. Electronic mail: gianfranco.gargano@ba.infn.it

[1]Cancer Facts & Figures, American Cancer Society, 2005.
[2]Cancer Facts & Figures, American Cancer Society, 1999.
[3]D. F. Yankelevitz, R. Gupta, B. Zhao, and C. I. Henschke, "Small pulmonary nodules: Evaluation with repeat CT preliminary experience," Radiology **212**, 561–566 (1999); D. F. Yankelevitz, A. P. Reeves, W. J. Kostis, B. Zhao, and C. I. Henschke, "Small pulmonary nodules: Volumetrically determined growth rates based on CT evaluation," *ibid.* **217**, 251–256 (2000).
[4]M. S. Brown, J. G. Goldin, S. Rogers, H. J. Kim, R. D. Suh, M. F. McNitt-Gray, S. K. Shah, D. Truong, K. Brown, J. W. Sayre, D. W. Gjertson, P. Batra, and D. R. Aberle, "Computer-aided lung nodule detection in ct: results of large-scale observer test," Acad. Radiol. **12**, 681–686 (2005).
[5]K. Peldschus, P. Herzog, S. A. Wood, J. I. Cheema, P. Costello, and J. Schoepf, "Computer-aided diagnosis as a second reader: Spectrum of findings in CT studies of the chest interpreted as normal," Chest **128**, 1517–1523 (2005).
[6]K. Suzuki, S. G. Armato III, F. Li, S. Sone, and K. Doi, "Massive training artificial neural network (MTANN) for reduction of false positives in computerized detection of lung nodules in low-dose computed tomography," Med. Phys. **30**, 1602–1617 (2003).
[7]M. N. Gurcan, B. Sahiner, N. Petrick, H.-P. Chan, E. A. Kazerooni, P. N. Cascade, and L. Hadjiiski, "Lung nodule detection on thoracic computed tomography images: Preliminary evaluation of a computer-aided diagnosis system," Med. Phys. **29**, 2552–2558 (2002).
[8]Y. Lee, T. Hara, H. Fujita, S. Itoh, and T. Ishigaki, "Automated detection of pulmonary nodules in helical CT images based on an improved template-matching technique," IEEE Trans. Med. Imaging **20**, 595–604 (2001).
[9]A. S. Roy, S. G. Armato III, A. Wilson, and K. Drukker, "Automated detection of lung nodules in CT scans: False positives reduction with the radial-gradient index," Med. Phys. **33**, 1133–1140 (2006).
[10]P. Raffy, C. I. Fetita, C. Beigelman-Aubry, F. J. Prêteux, S. A. Wood, and P. Grenier, *Evaluation of Computer-aided Detection Performance using Mathematically Simulated Lung Nodules*, in Proceedings International Conference on Computer Assisted Radiology and Surgery, CARS'04, International Congress Series (Elsevier, Amsterdam, 2004), Vol. 1268, pp. 935–940.
[11]R. Bellotti *et al.*, "Distributed medical images analysis on a GRID infrastructure," FGCS, Future Gener. Comput. Syst. **23**, 475–484 (2007).
[12]F. Fauci *et al.*, "A massive lesion detection algorithm in mammography," Phys. Medica **XXI**, 21–28 (2005); D. Cascio *et al.*, "Mammogram segmentation by contour searching and mass lesions classification with neural network," Trans. Nucl. Sci. **53**, 2827–2833 (2006); R. Bellotti *et al.*, "A completely automated CAD system for mass detection in a large mammographic database," Med. Phys. **33**, 3066–3075 (2006); C. S. Cheran *et al.*, "Detection and Classification of Microcalcification Clusters in Digital Mammograms," in Proceedings of IEEE Medical Imaging Conference, Rome, Italy, 16–22 Oct. 2004.
[13]G. Gargano, R. Bellotti, F. De Carlo, S. Tangaro, E. Tommasi, M.

Castellano, P. Cerello, S. C. Cheran, and C. Fulcheri, "A novel Active Contour Model algorithm for contour detection in complex objects," in Proceedings of the 2007 IEEE International Conference on Computational Intelligence for Measurement Systems and Applications, Ostuni, Italy, 27–29 June 2007.
[14]J. G. Ravenel, E. M. Scalzetti, W. Huda, and W. Garrisi, "Radiation exposure and image quality in chest CT examinations," AJR, Am. J. Roentgenol. **177**, 279–284 (2001).
[15]M. Kass, A. Witkin, and D. Terzopoulos, "Snakes: Active contour models," Int. J. Comput. Vis. **1**, 321–331 (1988).
[16]T. Jen-Chao, T. Shung-Tsang, L. Ching-Po, and S. Kai-Tai, "Real-time image tracking for automatic traffic monitoring and enforcement applications," Image Vis. Comput. **22**, 485–501 (2004).
[17]W. Kwok-Wai, L. Kin-Man, and N. Kit-Chong, "An accurate active shape model for facial feature extraction," Pattern Recognit. Lett. **26**, 2409–2423 (2005).
[18]J. K. Dong, "A fast and stable snake algorithm for medical images," Pattern Recognit. Lett. **20**, 507–512 (1999).
[19]T. W. Ridler and S. Calvard, "Picture thresholding using an iterative selection method," IEEE Trans. Syst. Man Cybern. **8**, 630–632 (1978).
[20]J. P. Ko and M. Betke, "Chest CT: Automated nodule detection and assessment of change over time preliminary experience," Radiology **218**, 267273 (2001).
[21]J. Hertz, A. Krogh, and R. G. Palmer, *Introduction to the Theory of Neural Computation* (Addison-Wesley, Reading, MA, 1991).
[22]D. E. Rumelhart and J. L. McClelland, *Parallel Distributed Processing* (MIT Press, Cambridge, MA, 1986), Vol. I.
[23]M. Stone, "Cross-validatory choice and assessment of statistical predictions," J. R. Stat. Soc. Ser. B (Methodol.) **36**, 111–147 (1974).
[24]J. A. Swets, "Measuring the accuracy of diagnostic systems," Science **240**, 1285–1293 (1988).
[25]J. A. Hanley and B. J. McNeil, "The meaning and use of the area under a receiver operating characteristic (ROC) curve," Radiology **143**, 29–36 (1982).